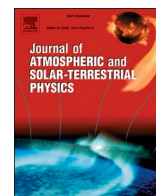


This work was written as part of one of the author's official duties as an Employee of the United States Government and is therefore a work of the United States Government. In accordance with 17 U.S.C. 105, no copyright protection is available for such works under U.S. Law. Access to this work was provided by the University of Maryland, Baltimore County (UMBC) ScholarWorks@UMBC digital repository on the Maryland Shared Open Access (MD-SOAR) platform.

Please provide feedback

Please support the ScholarWorks@UMBC repository by emailing [scholarworks-group@umbc.edu](mailto:scholarworks-group@umbc.edu) and telling us what having access to this work means to you and why it's important to you. Thank you.





# HYPERS simulations of solar wind interactions with the Earth's magnetosphere and the Moon

Yuri A. Omelchenko<sup>a,b,\*</sup>, Vadim Roytershteyn<sup>a</sup>, Li-Jen Chen<sup>c</sup>, Jonathan Ng<sup>d</sup>, Heli Hietala<sup>e</sup>

<sup>a</sup> Space Science Institute, Boulder, CO, USA

<sup>b</sup> Trinum Research, Inc., CA, USA

<sup>c</sup> NASA Goddard Space Flight Center, Greenbelt, MD, USA

<sup>d</sup> University of Maryland, College Park, MD, USA

<sup>e</sup> Imperial College, London, UK

## ARTICLE INFO

### Keywords:

Models  
Magnetosphere  
Kinetic  
Hybrid

## ABSTRACT

The hybrid simulations, where the ions are treated kinetically and the electrons as a fluid, seek to describe ion microphysics with maximum physical fidelity. The hybrid approach addresses the fundamental need for space plasma models to incorporate physics beyond magnetohydrodynamics. Global hybrid simulations must account for a wide range of both kinetic ion and whistler/Alfvén wave spatio-temporal scales in strongly inhomogeneous plasmas. We present results from two three-dimensional hybrid simulations performed with a novel asynchronous code, HYPERS designed to overcome computational bottlenecks that typically arise in such multiscale simulations. First, we demonstrate an excellent match between simulated lunar wake profiles and observations. We also compare our simulations with two other simulations performed with conventional (time-stepped) hybrid codes. Second, we investigate the interaction of the solar wind with the Earth's dayside magnetosphere under conditions when the orientation of the interplanetary magnetic field is quasi-radial. In this high-resolution simulation we highlight three-dimensional properties of foreshock perturbations formed by the backstreaming ions.

## 1. Introduction

Forecasting the behavior of the Earth's magnetosphere is one of the grand challenges of space physics research. The reliance of our society on space-based assets for telecommunication, weather monitoring, and surveillance drives the need for better understanding of the factors that control magnetosphere dynamics. The Earth's magnetosphere is a complex, nonlinear system, where many distinct physical processes operate across scales and couple together in different regions (Borovsky and Valdivia, 2018). A majority of existing physics-based global models employ magnetohydrodynamics (MHD) as the underlying framework for describing plasma dynamics. Such models are known to have mixed success in reproducing observations (Ridley et al., 2016). Kinetic physics of the solar wind-magnetosphere coupling has long been discussed as one of the important ingredients missing from such models. That is because kinetic effects often control mass and energy transport, especially in numerous magnetospheric boundary layers, such as the bow shock and the magnetopause. Kinetic effects are also clearly important

for describing the foreshock regions, dynamics of ionospheric outflows, and magnetic reconnection.

The potential significance of the kinetic effects has stimulated an extensive body of work aimed at constructing global models that go beyond MHD. Fluid models could be obtained by utilizing underlying theoretical approximations for describing plasma motion that average out certain scales. MHD is the most widely used and successful approximation of this type, but multi-fluid or extended fluid models have also been proposed (Raeder et al., 2003). Augmented fluid models, with better closures of moment equations, are also being pursued to improve the representation of kinetic physics (Wang et al., 2015, 2018). More sophisticated approximations of this type, such as the gyrokinetic approach (Brizard and Hahm, 2007), which has been successful in magnetic fusion energy applications, average out some degrees of freedom (e.g. particle gyro-motion). A more direct approach is to include microscopic physics only locally in selected regions of configuration space by embedding a kinetic solver within a large-scale fluid framework (Sugiyama and Kusano, 2007; Daldorff et al., 2014; Tóth

\* Corresponding author. Space Science Institute, Boulder, CO, USA.

E-mail address: [yurio@spacescience.org](mailto:yurio@spacescience.org) (Y.A. Omelchenko).

<https://doi.org/10.1016/j.jastp.2021.105581>

Received 29 May 2020; Received in revised form 22 December 2020; Accepted 4 February 2021

Available online 22 February 2021

1364-6826/© 2021 Elsevier Ltd. All rights reserved.



et al., 2016; Chen et al., 2017; Ho et al., 2018).

The focus of this paper is a particular approximation known in plasma physics as a quasineutral hybrid description. The electron inertial scales and radiation effects are removed from this approximation and microscopic ion physics is incorporated with maximum fidelity (Hewett, 1980; Harned, 1982; Winske et al., 2003). The hybrid approach, bridging scales between MHD and full plasma kinetics, has shown great promise in global magnetospheric and laboratory plasma applications. In many cases hybrid-PIC (Particle-in-Cell) (Winske et al., 2003) and hybrid-Vlasov (von Alfthan et al., 2014) magnetospheric models reveal significantly different plasma dynamics compared to fluid models, producing closer matches between simulation results and observations. This comes, however, at the expense of having to numerically handle a wide range of spatio-temporal scales (compared to MHD), which gives rise to daunting computational challenges in global three-dimensional (3D) simulations.

Below we discuss how some of these challenges have been overcome in a novel, asynchronous hybrid code, HYPERS (HYbrid Particle Event-Resolving Simulator) (Omelchenko and Karimabadi, 2012a). The goal is to provide a status update on the continuous development of HYPERS capabilities and discuss results from two challenging 3D problems performed here as case studies. Specifically 1) we compare results from lunar wake simulations to both observations and previous simulations to demonstrate the accuracy of HYPERS and reveal computational details that affect physical fidelity of hybrid simulations, and 2) we present results from a high-resolution 3D simulation of the solar wind interaction with the Earth's dayside magnetosphere and discuss our findings in the context of theory and available observational data.

## 2. Hybrid parallel event-resolving simulator (HYPERS)

HYPERS is an asynchronous, massively parallel hybrid code, which treats ions as particles and electrons as a massless quasineutral fluid in the Darwin (radiation-free) approximation (Omelchenko and Karimabadi, 2012a, 2012b). Compared with conventional hybrid codes, HYPERS implements a novel computational approach to simulation: Event-Driven Multi-Agent Planning System (EMAPS). EMAPS is a newer acronym that replaces a more general term, DES (Discrete-Event Simulation) used in previous HYPERS related publications to emphasize event-driven computation. This new acronym emphasizes self-adaptivity of asynchronous rule-based calculations compared to conventional DES. EMAPS, acting as an intelligent "Simulation Time Operating System", evolves the hybrid model in time via change prediction, detection and execution, rather than synchronous time stepping. EMAPS enables stable and accurate time advance of temporally disparate computational elements (particles, discretized variables, external models, etc) on their own local timescales, i.e. without forcing their global update at predetermined time steps. This property dramatically improves the fidelity and efficiency of multiscale hybrid simulations compared to synchronous time stepping, which makes EMAPS an excellent choice for modeling strongly coupled and inhomogeneous systems such as planetary magnetospheres. HYPERS has already performed challenging modeling tasks on massively parallel supercomputers with more than 100,000 cores. More sophisticated simulations will inevitably benefit from incorporating mesh refinement techniques and taking advantage of steady progress in computing power.

In HYPERS the global model of solar wind interactions with planetary bodies is initialized with a uniform (generally multiple ion species) plasma flow, which streams past a spherical conducting or resistive obstacle. This obstacle may represent an inner magnetospheric boundary with a magnetic dipole, or an unmagnetized body such as the Moon. In addition, ion outflows can be optionally enabled to study their impact on magnetospheric processes. The Earth radius, as well as the magnetopause position are typically scaled down in global hybrid simulations compared to their actual values. For instance, the characteristic proton

inertial length,  $\lambda_p$  in the solar wind is of order 100 km, the Earth radius is  $\sim 64\lambda_p$  and the magnetopause distance,  $R_{MP}$  is  $\sim (6 - 15)R_E \sim (400 - 1000)\lambda_p$ . The largest 3D HYPERS simulations to date used approximately  $1000 \times 2000 \times 2000$  cells and  $R_{MP} \sim 160\lambda_p$ . Earlier, detailed comparisons of global HYPERS simulations with simulations performed with a time-stepped hybrid code, H3D demonstrated the superior performance of HYPERS in terms of computing speed and numerical accuracy, with HYPERS producing less diffusive and less dispersive solutions (Omelchenko and Karimabadi, 2012a).

In the simulations discussed in this paper all external domain boundaries are considered to be absorbing for waves. This is implemented by introducing spatial layers where the plasma resistivity grows towards external boundaries. The domain boundaries in the solar wind direction (x-direction) are absorbing for particles. Other domain boundaries implement semi-reflective conditions that absorb highly energetic and back-streaming particles and reflect other particles. All particles are absorbed when they hit the obstacle boundary. Interplanetary (IP) shocks and solar wind discontinuities can be initialized in HYPERS by changing plasma injection parameters at the inflow boundary. Rotational discontinuities may be introduced by modifying the tangential electric field at the inflow boundary. Locally modified components of the Interplanetary Magnetic Field (IMF) tangential to the injection surface are then transported into the simulation domain by free streaming plasma. EMAPS automatically adjusts particle and field time steps in accordance with local conditions to maintain prescribed accuracy.

## 3. Lunar wake simulations

Recent spacecraft missions have effectively established the Moon as a unique plasma physics laboratory for studying universal processes at the scale of the ion inertial length. Many of these phenomena affect all planets, including the Earth. Kinetic ion simulations of solar wind interactions with the Moon are useful for both explaining observations and improving hybrid simulation models (Kallio et al., 2019; Holmström et al., 2012; Kallio, 2005), which are actively used for exploring the multiscale physics of planetary magnetospheres. Predictive capabilities of computational hybrid models strongly depend on their implementation details such as spatial-temporal discretizations of Maxwell's equations, equations of particle motion and particle-mesh coupling (interpolation) schemes. In addition, as we show below, physical fidelity of results may be greatly affected by a modeling method for treating low-density and vacuum regions where the standard hybrid model is not applicable.

Given the relative simplicity of the Moon's environment compared to the Earth's magnetosphere, as well as availability of numerous lunar wake observations, such as recorded by the Time History of Events and Macroscale Interactions during Substorms (THEMIS)/Acceleration, Reconnection, Turbulence and Electrodynamics of the Moon's Interaction with the Sun (ARTEMIS) spacecraft (Angelopoulos, 2011), lunar simulations present an excellent test bed for validating hybrid codes used in space plasma physics.

Below we compare HYPERS results with observations and results from similar 3D simulations of solar wind interactions with the Moon obtained with two other hybrid codes, namely a code used by Omid et al. (2019a) and the AMITIS code (Fatemi et al., 2017), used by Poppe (2019) in a comment on the former. The goal of all these studies is to accurately simulate physical phenomena recorded by the ARTEMIS P2 spacecraft during its crossing of the Moon's wake. In addition, a comparative analysis of three hybrid simulations serve the purpose of demonstrating the role of numerical effects in hybrid simulations.

In our study we use baseline solar wind parameters from the "Run-0" simulation by Omid et al. (2019a). We employ a resistivity model that treats the Moon and low-density plasma regions as highly resistive media with a resistivity,  $\eta \approx 2 \times 10^7 \Omega\cdot m$ , similar in magnitude to the



resistivity used in the AMITIS simulations (Fatemi et al., 2017). The purpose of this ad hoc resistivity model is to enable fast propagation of magnetic field in vacuum in the absence of the displacement current (radiation) term in the hybrid equations. In addition, a small constant value of resistivity,  $\eta = 10^2 \Omega \cdot m$  is applied inside plasma to smooth out noise. To avoid spurious features at wake edges, where the resistivity becomes discontinuous, we smooth the resistivity by applying a spatial filter.

Following (Omidi et al., 2019a) the x and y axes in our lunar wake simulations are opposite to the corresponding GSE axes, and the orientation of the z axis is the same. The solar wind streams along the x direction. We assume that the interplanetary magnetic field with a strength,  $B_0 = 9nT$  lies in the x-y plane with a cone angle of  $30^\circ$ :  $\mathbf{B}_0 = [7.8, -4.5, 0]nT$ . The solar wind is composed of protons only: the proton number density,  $n_0 = 3.5cm^{-3}$ , the proton speed,  $V_0 = 610km/s$ , and the proton and electron temperatures,  $T_p = T_e = 22eV$ . For the chosen parameters the Moon's radius,  $R_M \approx 14\lambda_p$  and the Mach number,  $M_A = V_0/V_A \approx 5.8$ , where  $\lambda_p = c/\omega_p$  is the proton inertial length and  $V_A$  is the Alfvén speed,  $V_A = B_0/\sqrt{4\pi n_0 m_p}$  ( $\omega_p$  and  $m_p$  are the proton plasma frequency and mass, respectively).

To establish convergence of numerical results with respect to mesh resolution we have conducted simulations using two different meshes,  $\Delta x = \Delta y = \Delta z = \lambda_p$  ( $100 \times 100 \times 100$  cells) and  $\Delta x = \Delta y = \Delta z = 0.5\lambda_p$  ( $200 \times 200 \times 200$  cells). These simulations were initialized with 100 macro-particles per cell and run for a time period  $\approx 2L/V_0$  ( $L$  is the domain length in the x-direction), long enough to establish a time-steady profile of the lunar wake. The electric field at the upstream boundary is set to the unperturbed solar wind value,  $\mathbf{E}_0 = -\mathbf{V}_0 \times \mathbf{B}_0$  and computed self-consistently at other boundaries. Tangential components of self-generated magnetic field are set to zero at the upstream boundary and remain floating at other boundaries. Note that the HYPERS solver automatically takes into account nonuniform resistivity in the lunar wake simulations, producing field time step distributions shown in Fig. 1.

Omidi et al. (2019a) explored simulation setups where in addition to bulk thermal protons ("Run-0") the solar wind was also initialized with small populations of energetic protons. The energetic ions were claimed to dominate solar wind interactions with the Moon. These conclusions were challenged by Poppe (2019), followed by a reply by Omidi et al. (2019b). Our study focuses on three questions brought up in this discussion: 1) Is the presence of energetic ions in the solar wind essential for explaining the observed lunar wake structure, and most notably its magnetic field profile? 2) Is the compressional wake structure simulated by Omidi et al. (2019a), but not observed in the AMITIS simulations (Poppe, 2019), physical? 3) How well can hybrid simulations estimate the amplitude of the magnetic rarefaction wake during the inbound and

outbound paths of the ARTEMIS spacecraft trajectory?

Below we present our results in a form convenient for critical comparisons with simulations (Omidi et al., 2019a), (Poppe, 2019) and observations. Fig. 2 matches magnetic field magnitudes in our simulations, as a function of spacecraft transit time, with observations discussed in Omidi et al. (2019a). Fig. 3 contains plasma density and magnetic field magnitude snapshots (cross-cuts) from our higher-resolution run. This figure can be directly compared with Fig. 2 in Poppe (2019) and similar figures in Omidi et al. (2019a). Fig. 2 can also be directly compared to Fig. 3 in Poppe (2019) and similar figures in Omidi et al. (2019a).

We further evaluate our simulation results in a step-by-step fashion with a focus on the three science questions formulated above.

**Q1: Magnetic field profile.** As noted by Poppe (2019) the hybrid model (Omidi et al., 2019a) lacks a vacuum resistivity model. Though details of their resistivity model are unclear, Omidi et al. (2019b) confirmed they did not use a large resistivity in the wake region where the hybrid model breaks down in the absence of plasma. We concur with (Poppe, 2019) that such a model is necessary for lunar wake studies since it provides a physical mechanism for fast magnetic field propagation in vacuum in the absence of radiation effects. In the absence of this "vacuum" resistivity, Omidi et al. (2019a) obtained an unphysical magnetic field profile in their baseline case ("Run-0", no energetic ions). Adding populations of energetic ions into the solar wind then resulted in simulation profiles that matched the observational data more closely. Based on these findings Omidi et al. (2019a) concluded that energetic ions play a dominant role in explaining the observed magnetic field magnitudes in the Moon's wake. The comment by Poppe (2019), however, pointed out that the lunar wake in the baseline case in Omidi et al. (2019a) was modeled incorrectly. In other runs Omidi et al. (2019a) initialized the solar wind with energetic ions that formed a low-density plasma in the wake, capable of supporting fast magnetic propagation. Not surprisingly, magnetic field amplitude profiles in those simulations were found to be more realistic (Poppe, 2019).

In our simulations the vacuum resistivity is chosen to be large enough to enable converging results. These simulations convincingly prove (see Fig. 2) that one can accurately simulate the observed magnetic field magnitudes in the Moon's wake without assuming the presence of energetic ions in the solar wind. We generated these wake profiles along a path obtained by combining three segments of the ARTEMIS spacecraft trajectory. The data are then interpolated from simulation cells that are the closest to points chosen in this path. In the simulation frame of reference the Moon-centered coordinates of the chosen four points of the ARTEMIS trajectory in  $R_M$  units are as follows: 22:30 (0.14,-1.95,-0.63), 23:00 (1.31,-0.81,-0.13), 23:30 (1.55,0.85,0.44), 24:00 (1.02,2.20,0.83).

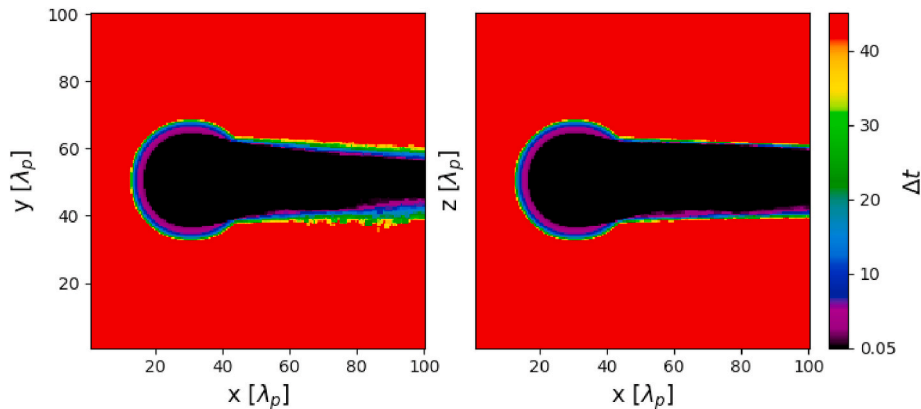
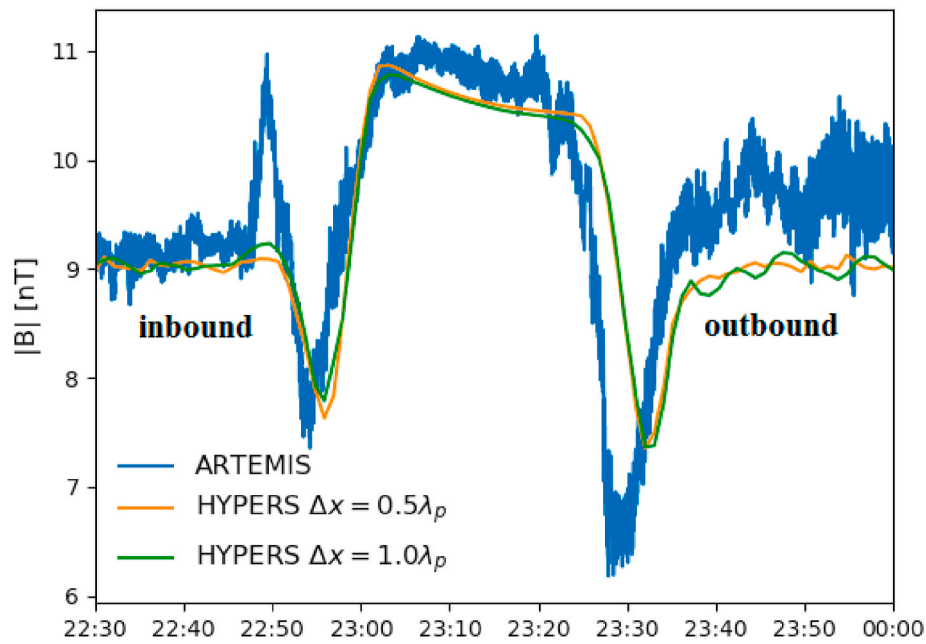
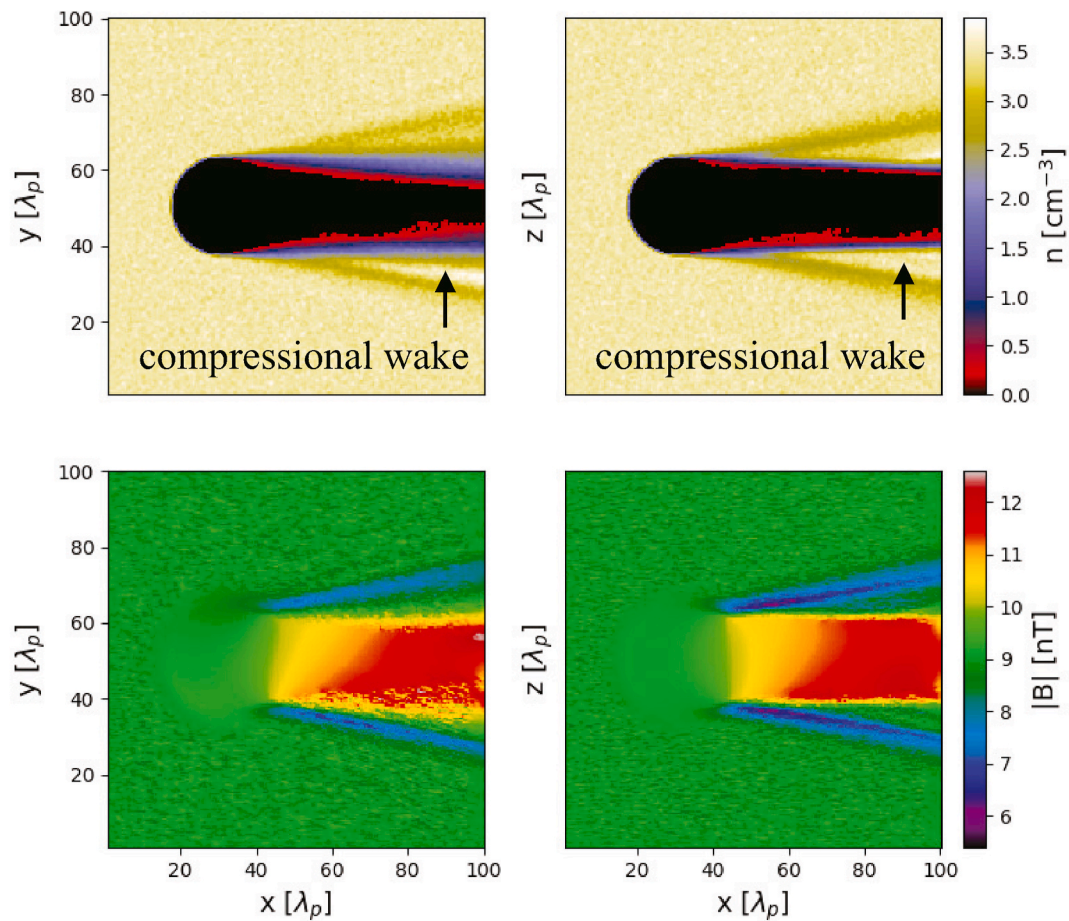


Fig. 1. Time steady distributions of field time steps normalized to the inverse proton plasma frequency,  $\omega_p^{-1}$  in two central planes, x-y and x-z in the 3D HYPERS lunar wake simulation with  $\Delta x = 0.5\lambda_p$ . The black color corresponds to small time steps taken by the field solver in cells where the plasma density falls below the cutoff density ( $\approx 0.18cm^{-3}$ ). (For interpretation of the references to color in this figure legend, the reader is referred to the Web version of this article.)





**Fig. 2.** Comparison of the ARTEMIS P2 magnetic field magnitude profile (Omid *et al.*, 2019a) with results from two HYPERS lunar simulations with different mesh resolutions.



**Fig. 3.** Time steady plasma density and magnetic field magnitude in two central planes, x-y and x-z in the HYPERS lunar simulation with  $\Delta x = 0.5\lambda_p$ .



**Q2: Compressional effects.** Omid et al. in their reply (Omid et al., 2019b) to the comment by Poppe (2019) acknowledge the importance of describing vacuum in the Moon's hybrid simulations as a highly resistive medium. At the same time they note that the AMITIS simulations (Poppe, 2019) do not show a compressional wake in the Moon's tail structure. Indeed, Fig. 2 in Poppe (2019) lacks this feature. Moreover, a conclusion is made in Poppe (2019) that compressional effects in the wake observed in Omid et al. (2019a) may be transient in nature since the simulation (Omid et al., 2019a) may not have reached a steady state. In their turn, Omid et al. (2019b) refer to the presence of this feature in their simulations as an evidence in support of their conclusion that the Moon's wake is dominated by energetic protons with large Larmor radii. We note, however, that the compressional wake can be also observed in our steady state solutions (see Fig. 3), obtained in the absence of energetic ions in the solar wind. Moreover, similar compressional effects are also observed in our lower-resolution simulation, as well as in earlier simulations by Poppe et al. (2014). The perturbations in the lunar wake arise from a combination of compressional and Alfvénic effects (Zhang et al., 2016). Omid et al. (2019b) show that additional data from the ARTEMIS spacecraft demonstrate that the compressional wake is part of the lunar tail structure and not associated with crustal fields.

**Q3: Diamagnetic depressions.** Omid et al. (2019b) correctly note that the AMITIS code underestimates the amplitude of the rarefaction magnetic signal during the outbound part of the ARTEMIS spacecraft trajectory. They, however, proceed with using this fact as an additional argument in support of their theory of energetic ion dominance in the lunar wake. Indeed, in Poppe (2019) this feature in Fig. 3 is significantly damped compared to the observational data. Omid et al. (2019b) ultimately conclude that it is not clear how this result can be further improved without modifying the resistive vacuum model. The profiles of magnetic field obtained in our simulations are shown in Fig. 2. They do a much better job matching the observations in question than the magnetic field profiles obtained by Omid et al. with energetic ions, which show significant variations in signal magnitude and profile shapes. Therefore, we conclude that the resistive wake model is more consistent with the ARTEMIS observations than the model with energetic ions, proposed by Omid et al. (2019a, 2019b).

Notably absent from all three simulations is a strong paramagnetic enhancement observed by the ARTEMIS P2 spacecraft during the inbound part of its trajectory, as seen in Fig. 2. Although HYPERS shows transient compressional magnetic field enhancements at the same location at early simulation times, this response eventually becomes small in the steady state, as seen in this Figure. Not all ARTEMIS lunar wake crossings observe such strong magnetic field enhancements at this location. For instance, ARTEMIS data shown in Fig. 2 in Omid et al. (2019b) demonstrate small paramagnetic responses, similar in magnitude to ones observed in our simulations. Therefore, we hypothesize that transient solar wind effects, such as variations in solar wind density and velocity, may play a role in producing and controlling this feature. Lunar crustal magnetic fields have also been suggested as an alternative explanation for the observed paramagnetic enhancement [e.g. (Halekas et al., 2008)]. These effects, however, are not taken into account in our simulations.

To summarize, HYPERS simulations of the Moon's wake demonstrate that the observed wake profiles can be accurately predicted by hybrid simulations that represent the vacuum portion of the model with a highly resistive medium, as earlier shown by Poppe (2014), Poppe et al. (2014). In particular, quantitative results produced in HYPERS simulations with a vacuum resistivity model and no energetic ions are in an excellent match with the ARTEMIS observations.

#### 4. Simulation of solar wind interaction with the dayside magnetosphere

In this section we describe a global 3D HYPERS simulation of the

solar wind interaction with the Earth's dayside magnetosphere. The overall geometry and methodology of this simulation setup resemble those used in many prior studies in 2D (Blanco-Cano et al., 2009; Karimabadi et al., 2006, 2014; Lin, 2003; Omid et al., 2005; Swift, 1996; von Alfthan et al., 2014) and 3D (Karimabadi et al., 2011; Lin and Wang, 2005; Lu et al., 2020). At the same time, the unique computational properties of HYPERS enable us to conduct large-scale, high-quality simulations with relatively modest computational costs. Specifically, in this simulation the computational domain of size  $L_x \times L_y \times L_z = 1024 \times 2048 \times 2048 \lambda_p$  is discretized with  $n_x \times n_y \times n_z = 512 \times 1024 \times 1024$  cells arranged in a uniform Cartesian mesh.

The solar wind proton plasma continuously streams from the injection (left) boundary with an initial speed,  $V_0 = -10V_A$  in the negative GSM  $x$  direction. The interplanetary magnetic field,  $\mathbf{B}_0$  is in  $x-z$  plane and inclined at an angle of  $21.6^\circ$  with respect to the  $x$  axis, with a positive GSM  $z$  component. The solar wind is initialized with the following dimensionless parameters characteristic of a specific observational event:  $c/V_A = \omega_p/\Omega_{cp} = 7800$  ( $\Omega_{cp}$  is the proton cyclotron frequency computed with respect to  $B_0$ ), and ion and electron betas,  $\beta_i = 0.6$ , and  $\beta_e = 1.6$ , respectively. As in the Moon's study above, an adiabatic equation of state with  $\gamma = 5/3$  is used for fluid electrons.

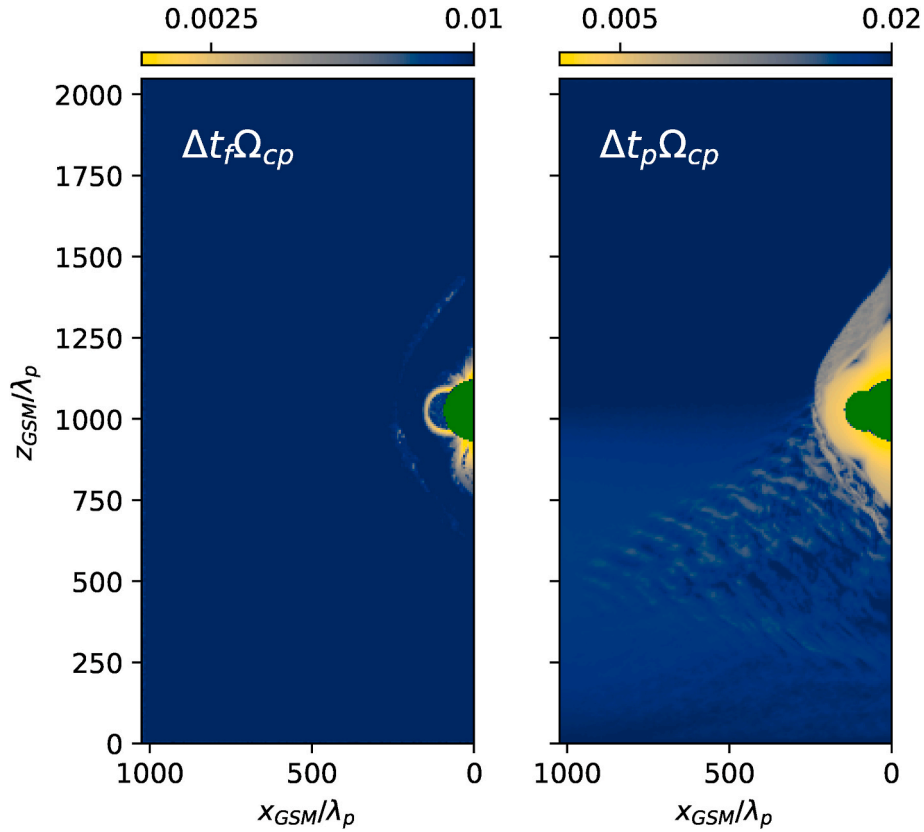
The Earth's magnetic field is represented by a dipole located at the center of the right simulation boundary,  $x_{GSM} = 0$ . The strength of the dipole is rescaled to yield a reference magnetopause standoff distance,  $D_p = 160\lambda_p$ . The actual distance to the magnetopause is larger. For example, at time  $t\Omega_{cp} \approx 300$ , when the magnetosphere is fully developed, the magnetopause standoff distance is approximately  $215 \lambda_p$  at the subsolar point, while the distance to the bow shock is approximately  $255 \lambda_p$ . A perfectly conducting obstacle of radius  $R_0 = 92\lambda_p$  surrounds the dipole. Below we discuss the most salient features observed in this simulation. Note that we use the GSM coordinates in this discussion.

Fig. 4 illustrates the asynchronous nature of HYPERS time advance in this 3D magnetospheric simulation. It demonstrates an instantaneous distribution of self-driven local field (left panel) and particle (right panel) time steps. In contrast to traditional explicit algorithms, where global time steps would have to be smaller or equal to the minimum value found in these two distributions, the HYPERS algorithm provides a significant degree of optimization by enabling local time steps to vary in space and time through event-driven adaptation to physical features dynamically developing in the simulation. This makes HYPERS simulations of the Earth's magnetosphere numerically stable, physically accurate and computationally efficient.

It is well known that the quasi-radial IMF conditions considered in this study lead to a highly dynamic interaction of the solar wind with the magnetosphere, which are driven, in part, by low frequency perturbations formed in the ion foreshock by instabilities associated with the backstreaming ions. These perturbations can grow to large amplitudes, giving rise to a multitude of nonlinear phenomena, such as steepened fronts referred to as shocklets, short large-amplitude magnetic structures (SLAMS), and cavitons (Burgess et al., 2005). Such highly energetic dayside transient phenomena as Magnetosheath High-Speed Jets (HSJs) are also associated with quasi-radial IMF conditions (Plaschke et al., 2018).

The overall morphology of foreshock perturbations in this 3D simulation is illustrated by Fig. 5. Similarly to results from previous 2D hybrid simulations (Strumik et al., 2015) (see also (Lin, 2003; Blanco-Cano et al., 2009; Karimabadi et al., 2014; Turc et al., 2018)), low-frequency waves in the foreshock exhibit properties resembling the so-called 30s ULF waves. In particular, they are formed as slightly oblique perturbations in an extended foreshock region. In the simulation frame of reference, these perturbations are observed as left-hand polarized compressional waves with wavelengths of the order of  $100 \lambda_p$  and frequencies of approximately  $0.5\Omega_{cp}$ , corresponding to the period of 32–33 s, assuming the reference magnetic field of 4 nT. In the solar wind frame of reference, however, these perturbations become





**Fig. 4.** Spatial distribution of field (left) and particle (right) time steps in a global simulation of the solar wind interaction with the Earth's magnetosphere. The time steps are normalized to proton cyclotron frequency  $\Omega_{cp}$ . The GSM coordinates are used here and in the subsequent figures illustrating the simulation of solar wind interaction with the Earth's magnetosphere.

right-hand polarized and propagate upstream.

While the foreshock fluctuations have a finite perpendicular wavelength with respect to the background magnetic field, a visual inspection indicates that they tend to acquire a large-scale transverse structure as they steepen while being convected towards the bow shock. Close to the bow shock, the characteristic size of this “super-structure” becomes comparable to the size of the foreshock region. This conclusion is generally consistent with estimates of the correlation length based on observations (Archer et al., 2005). The fluctuations are observable in the region extending approximately  $1000 \lambda_p$  upstream from the bow shock, a scale which is comparable to the size of the simulation domain and could likely be larger if the domain is extended.

To further illustrate properties of the ion foreshock perturbations, Fig. 6 shows profiles of the density, parallel temperature, magnetic field, and ion velocity in a 2D  $x - z$  plane passing through the sub-solar point (at  $y = 1024 \lambda_p$ ). In addition, a 1D cut (see a dashed line in the rightmost panel) produces profiles of  $n$ ,  $B$ , and  $V$  in Fig. 7. It is clear that the fluctuations are mildly compressible at significant distances from the shock, with amplitudes  $\delta|B|/B_0 \sim 0.1 - 0.2$ . Furthermore, their wavefronts have a small, but finite angle with respect to the ambient magnetic field. A field-aligned beam of backstreaming ions, evident in  $T_{\parallel}$  and  $|V|$  plots, is present at the edge of the foreshock (Blanco-Cano et al., 2009) and appears to generate waves at somewhat larger angles than those inside the foreshock. These waves steepen as they are convected towards the bow shock, as is most clearly evident in the  $B_y$  component of the magnetic field (see second panel of Fig. 7). Closer to the bow shock the fluctuations become highly compressible. The fluctuation amplitudes reach levels comparable to the solar wind magnetic field,  $\delta|B|/B_0 \sim 1$ , with density fluctuations (mostly depressions) being as large as 50%.

Frequency spectra of magnetic fluctuations are shown in Fig. 8. Each spectrum is computed by performing the Fast Fourier Transform (FFT) of

a time series collected at a fixed location in the simulation domain. The positions of such “control points” (CPs) are indicated in the leftmost panel of Fig. 6 by red dots, with numbers corresponding to the labels used in Fig. 8. Fluctuations are formed with frequencies approximately  $\omega \sim 0.5 \Omega_{cp}$ , as evidenced by a well-defined peak observed at control point 0. Closer to the bowshock (control point 1), the spectra broaden significantly, presumably due to the nonlinear character of the structures. Interestingly, detectable fluctuations are observed in a broad range of frequencies, as could be deduced by comparing spectra collected inside of the foreshock with those collected in the solar wind (control point 2).

In the quasi-parallel regions inside the magnetosheath, the fluctuation level increases further. Here the spectra are generally consistent with a Kolmogorov power law, although a limited cadence of the simulation output and a relatively small duration of the time series allow only a crude estimate of the spectra. The turbulence level is significantly lower in the quasi-perpendicular regions of the magnetosheath (control point 4).

While the highlighted features of foreshock perturbations bear a significant resemblance to those obtained in 2D simulations, the 3D geometry enables much more complex flow patterns and draping of magnetic field compared to 2D. One interesting aspect of the transition from the 2D to 3D geometry is to understand how this affects statistics and properties of various nonlinear structures in the foreshock and magnetosheath. In general, statistical information, such as occurrence rates, characteristic sizes, or correlations between various parameters could be obtained from observations. However, because observations are usually collected by a single spacecraft along its trajectory (at best by a few spacecraft in multi-spacecraft missions), the insight into the shape of various structures yielded by 3D kinetic simulations is of great interest. Below we present an example of such an analysis.



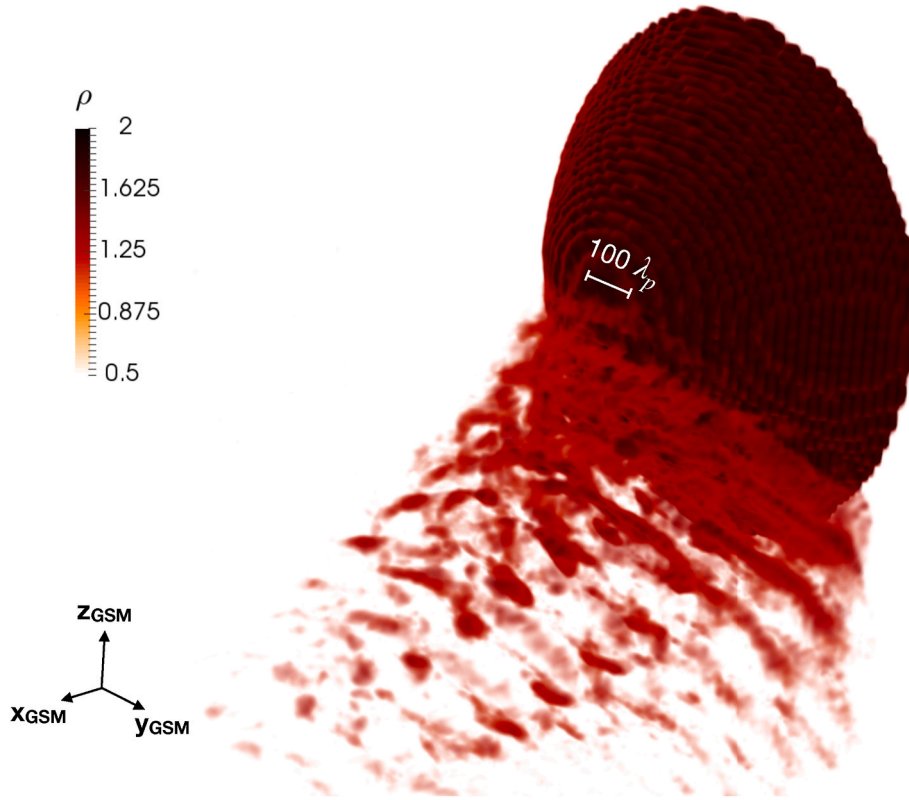


**Fig. 5.** Volumetric rendering of the plasma density in a global 3D HYPERS simulation of the solar wind interaction with the dayside magnetosphere. The large-scale perturbations excited by backstreaming ions in the ion foreshock are clearly visible. The upper limit for color scale is chosen to be twice the solar wind density, which highlights the bow shock surface. (For interpretation of the references to color in this figure legend, the reader is referred to the Web version of this article.)

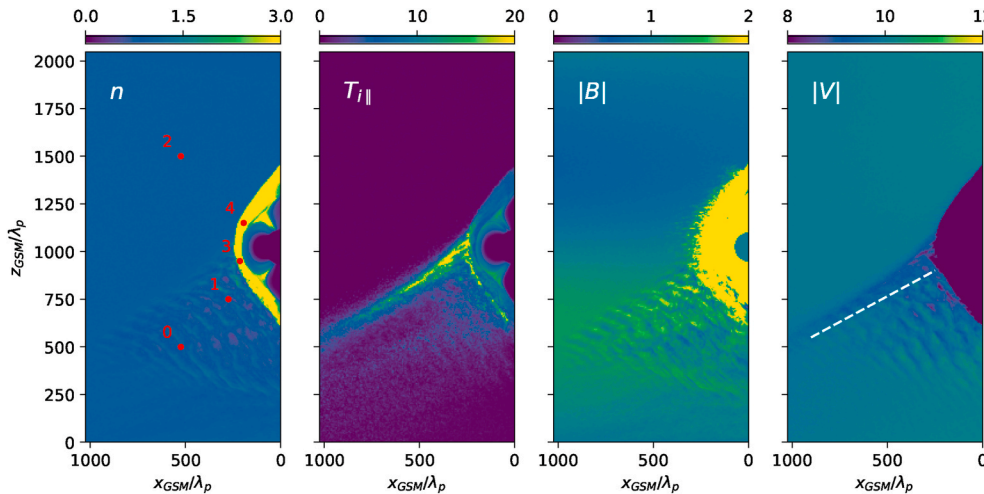


**Fig. 6.** Mid-plane 2D cuts illustrating the ion foreshock structure in a 3D large-scale HYPERS simulation of the solar wind interaction with the dayside magnetosphere. Left to right: the plasma density  $n$ , parallel ion kinetic temperature  $T_{\parallel}$ , magnitude of the magnetic field  $|B|$ , and ion velocity  $|V|$ . The red numbered dots on the left panel indicate locations of control points where the spectra shown in Fig. 8 were collected. The dashed line in the right panel shows the 1D cut used in Fig. 7. (For interpretation of the references to color in this figure legend, the reader is referred to the Web version of this article.)

As already apparent from Fig. 7, regions of significant simultaneously reduced magnitudes of the magnetic field and density embedded into foreshock perturbations are present in the simulation described here. Similar structures, termed foreshock cavities or cavitons, have been extensively studied in the previous 2D simulations (Blanco-Cano et al., 2009, 2018; Lin, 2003; Omid, 2007) and identified in observations as well (Kajdić et al., 2013) and references therein]. Fig. 9 illustrates several structures with significant reductions in the magnetic field and density (identified here by a rather strict condition  $n < 0.5n_0$  and  $|B| < 0.05B_0$ ) found in the simulation close to the bowshock. They have sizes ranging from the mesh scale to tens of ion inertial lengths, although mesh-scale structures were excluded from Fig. 9.

Panels c) and d) show typical profiles of the magnetic field and density across one of these structures. They demonstrate a significant depression in  $|B|$  and  $n$  and a substantial simultaneous increase in the ion temperature. Such an increase may appear to violate the caviton identification criterion used for example by Kajdić et al. (2013). However, the kinetic temperature shown here is a second moment of the velocity distribution and as such is sensitive to the presence of super-thermal particles, which are typically observed inside cavitons (Schwartz et al., 2006). Furthermore, increased ion temperatures inside some depressions have been reported in 2D simulations (Lin, 2003; Omid et al., 2013), especially for structures interacting with the shock and transitioning into Spontaneous Hot Flow Anomalies (Omid et al., 2013).



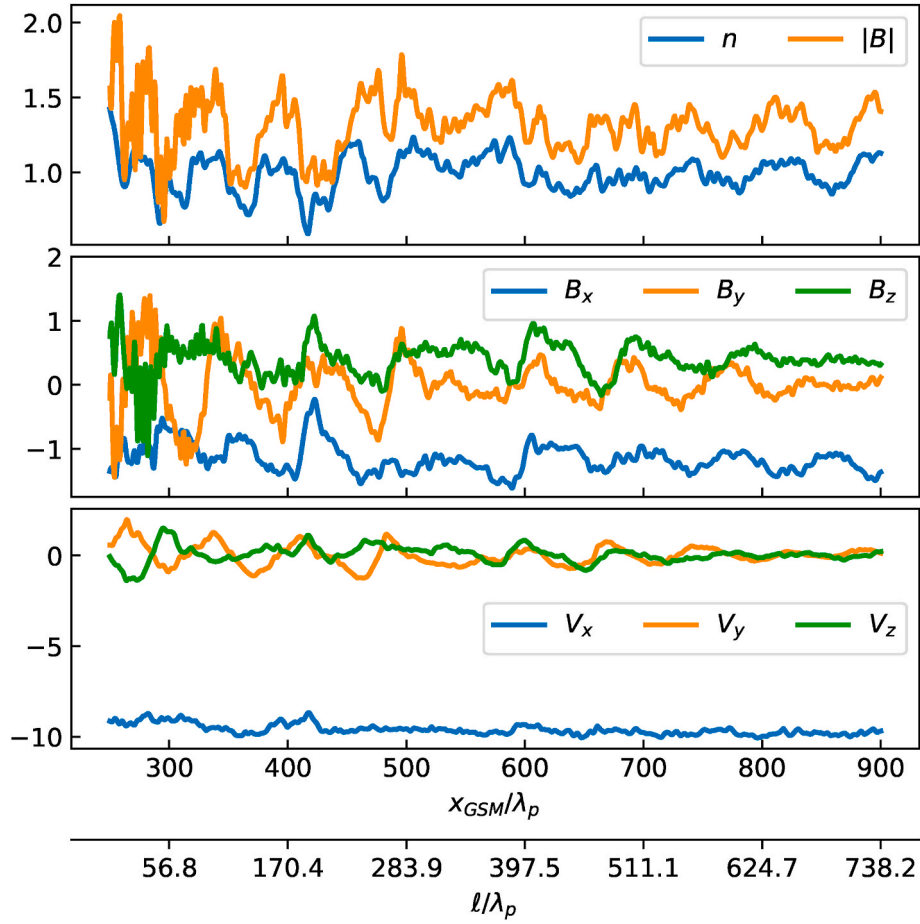


**Fig. 7.** Profiles of the plasma density and magnetic field magnitude (top), magnetic field components (middle) and velocity components (bottom) along the 1D cut indicated in the right panel of Fig. 6. The second horizontal axis shows distance  $\ell$  along the cut.

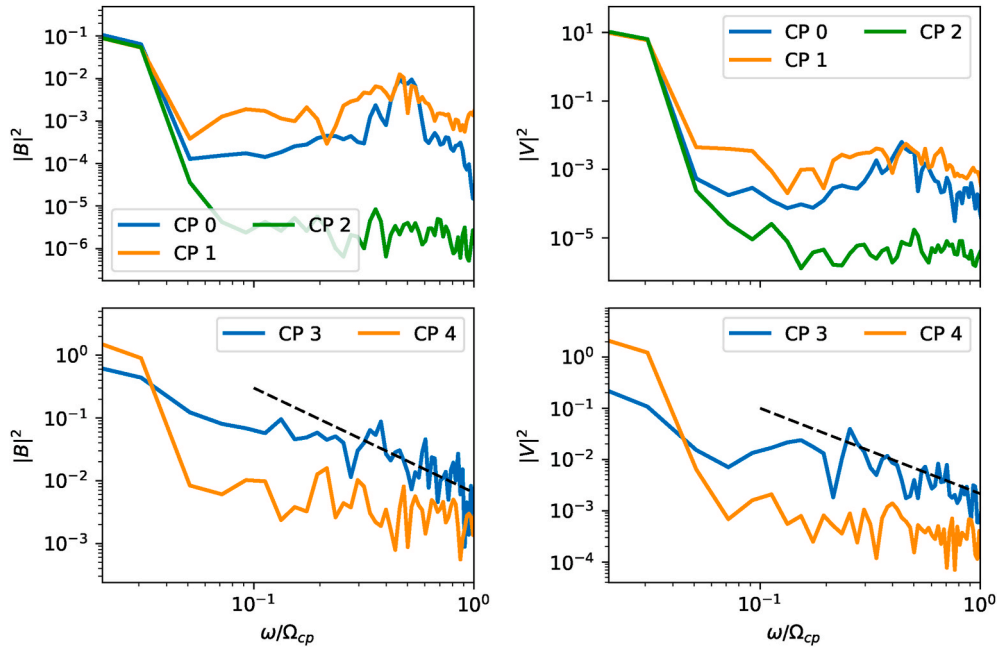


**Fig. 8.** Frequency spectra of the magnetic (left column) and velocity (right column) fluctuations at 5 control points (CP) indicated by red dots in Fig. 6. CPs 3 and 4 are located in the magnetosheath, while CPs 0–2 are outside the bowshock. For reference, the Kolmogorov scaling  $\omega^{-5/3}$  is indicated in the bottom two panels by the dashed line. (For interpretation of the references to color in this figure legend, the reader is referred to the Web version of this article.)



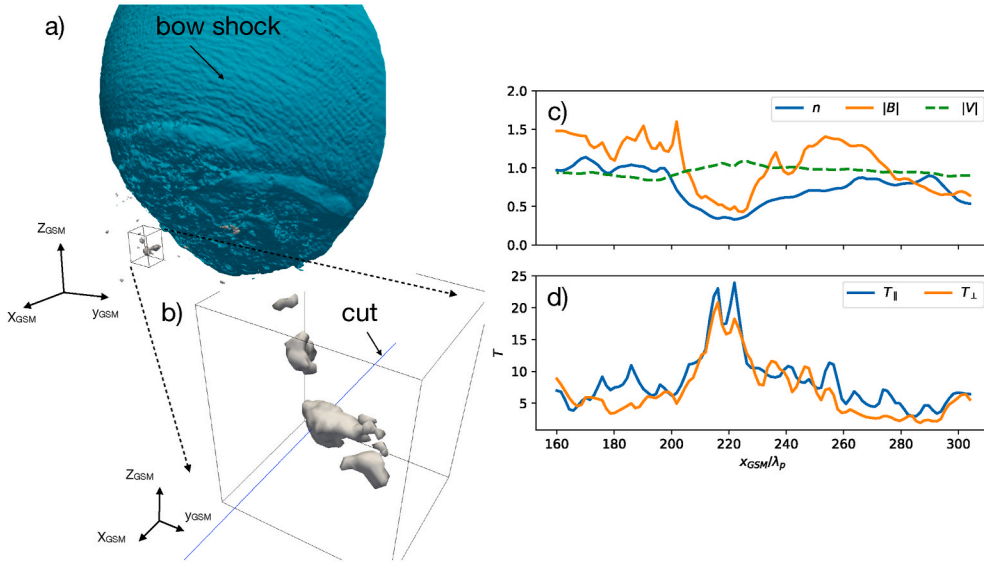


**Fig. 9.** An example of simulation structures characterized by correlated significant depressions of the magnetic field and plasma density: a) a shock surface (identified as an isosurface of constant density  $n = 2.5n_0$ ) and several structures highlighted by light grey surfaces. The box indicates a region of the simulation domain,  $l_x \times l_y \times l_z = (50 \times 60 \times 75)\lambda_p$  zoomed into in panel b); panels c) and d) show profiles of the magnetic field, density, and temperature along a 1D cut passing through the structure as indicated in panel b).

## 5. Summary

As of today, MHD is predominantly used for global physics-based modeling of the Earth's magnetosphere. Its success comes at the expense of reduced physics compared to more sophisticated kinetic models that compute detailed velocity distributions of plasma species (such as the ions in the hybrid models) and advance electromagnetic fields and particles on finer spatial meshes and faster time scales. However, under many solar wind and IMF conditions observed fields and plasma dynamics cannot be reproduced by MHD and empirical models. Foreshock turbulence, direct solar-wind ion injections into the cusp, ionospheric ion outflows energized to ring current energies, cascading of large-scale field-aligned currents into kinetic scales, solar wind-Moon interactions and magnetic reconnection are just a few examples where kinetic effects are essential for interpreting spacecraft data.

Global hybrid simulations, however, must account for a wide range of ion kinetic and cyclotron scales and spatio-temporal scales arising due to short-wavelength waves (whistlers). These short-wavelength scales play an important role in driving instabilities and turbulence, as well as influencing ion velocity distributions, as confirmed by the numerous observations. In order to adequately describe these “meso-scale” effects the hybrid simulations have to resolve the ion inertial length,  $\lambda_p \approx 1/60R_E$  ( $R_E$  is the Earth radius) and fast whistler time scales  $\sim 0.1$  s in the near-Earth region characterized by strong magnetic fields and low plasma density. Further, robust hybrid codes must be able to accurately account for dynamic turbulent patterns that emerge in global simulations under the influence of different solar wind drivers. The most notable feature that makes HYPERS different from other hybrid codes is its event-based approach to time integration. It enables stable and accurate time advance of particles and fields in a self-adaptive manner, on their own timescales. In this paper we have discussed results from 3D simulations of the lunar wake and the Earth's foreshock performed with HYPERS.

The lunar wake study serves two purposes. First, we regard it as a suitable 3D HYPERS model validation exercise, where we demonstrate a good agreement of our results with the ARTEMIS magnetic field data. Second, this study resolves a disagreement on physical effects that control lunar wake structures (in particular magnetic field profiles) observed by the ARTEMIS spacecraft (Omid et al., 2019a, 2019b; Poppe, 2019). We have confirmed that various aspects of these observations can be reproduced with accuracy using a proper resistive vacuum model, as has been earlier suggested by Poppe (2019), i.e., without

having to assume the presence of energetic ions in the solar wind, as argued by Omid et al. (2019a, 2019b). In particular, the HYPERS simulations, which approximate the Moon and wake as highly resistive media and use a standard solar wind model, match the magnetic field profile in the central lunar tail better than the simulations with energetic protons (Omid et al., 2019a) and the simulations performed with the AMITIS code (Poppe, 2019).

In the second part of this paper we have investigated a response of the Earth's dayside magnetosphere to quasi-radial IMF solar wind conditions. This simulation has resolved the 3D details of ultra-low-frequency (ULF) wave turbulence generated at the ion foreshock, as well as the concomitant plasma structures, consistent with observations. We have presented an analysis of these 3D foreshock cavities, which have been previously studied only in two dimensions. We also characterize the ULF waves driven by the backstreaming ions in the foreshock, and demonstrate turbulent spectra at different control points.

For reference, below we provide approximate computational costs of the simulations discussed in this paper. The lunar wake simulations are relatively straightforward to perform with hybrid codes. For this type of simulation the main numerical difficulty is associated with a large vacuum resistivity that imposes small time steps in the wake. The wake dynamically grows in time and eventually occupies a sizeable part of the computational domain. Therefore HYPERS cannot produce significant speedups in this setup. The coarse mesh run ( $100 \times 100 \times 100$  cells) took approximately 1.7 h on 448 parallel cores of Intel Xeon E5-2680v4 processors on the NASA Pleiades supercomputer. The fine mesh ( $200 \times 200 \times 200$  cells) run took approximately 10 h on 3584 cores. The large magnetospheric run, characterized by a significant inhomogeneity of field and particle time scales, took approximately 22 h on 131,072 cores of much older AMD 6276 “Interlagos” CPUs on the Blue Waters supercomputer.

The HYPERS code has undergone a number of important modifications since its original version was published (Omelchenko and Karimabadi, 2012a). The new features have improved the numerical accuracy and performance of HYPERS simulations. For instance, a dramatic improvement in numerical accuracy has resulted from implementing a second-order asynchronous correction in the field solver that identically preserves  $\nabla \cdot \mathbf{B} = 0$ . We have also implemented other important capabilities that enable us to concentrate computing power on compute-intense regions of a simulation domain and dramatically reduce the number of mesh cells in global simulations.

The results obtained in this paper establish firm grounds for further, more accurate 3D hybrid simulations of the Earth's magnetosphere and



other space bodies. A more thorough analysis of the plasma features observed in the Earth's foreshock, as well as algorithmic details of recent HYPERS code modifications, will be presented in separate publications.

### Declaration of competing interest

The authors declare that they have no known competing financial interests or personal relationships that could have appeared to influence the work reported in this paper.

### Acknowledgments

This work was supported by NASA Grant NNX17AI45G and NASA Grant 80NSSC19K0838. The lunar wake simulations were performed on the Pleiades supercomputer at NASA's Ames Research Center. The simulations discussed in Section 4 were conducted as a part of the Blue Waters sustained-petascale computing project supported by the National Science Foundation (awards OCI-0725070 and ACI-1238993) and the state of Illinois. Blue Waters is a joint effort of the University of Illinois at Urbana-Champaign and its National Center for Supercomputing Applications. The Blue Waters allocation was provided by the National Science Foundation through PRAC award 1614664.

The authors express their sincere gratitude to Vassilis Angelopoulos for providing the ARTEMIS data used in Fig. 2.

### References

- Angelopoulos, V., 2011. The ARTEMIS mission. *Space Sci. Rev.* 165 (1–4), 3–25. <https://doi.org/10.1007/s11214-010-9687-2>.
- Archer, M., Horbury, T.S., Lucek, E.A., Mazelle, C., Balogh, A., Dandouras, I., 2005. Size and shape of ULF waves in the terrestrial foreshock. *J. Geophys. Res.* 110, A05208. <https://doi.org/10.1029/2004JA010791>. <http://doi.wiley.com/10.1029/2004JA010791>.
- Blanco-Cano, X., Omid, N., Russell, C.T., 2009. Global hybrid simulations: foreshock waves and cavitons under radial interplanetary magnetic field geometry. *J. Geophys. Res.: Space Physics* 114, 1–14. <https://doi.org/10.1029/2008JA013406>.
- Blanco-Cano, X., Battarbee, M., Turc, L., Dimmock, A.P., Kilpua, E.K.J., Hoilijoki, S., Ganse, U., Sibeck, D.G., Cassak, P.A., Fear, R.C., Jarvinen, R., Juusola, L., Pfau-Kempf, Y., Vainio, R., Palmroth, M., 2018. Cavitons and spontaneous hot flow anomalies in a hybrid-Vlasov global magnetospheric simulation. *Ann. Geophys.* 36, 1081–1097. <https://doi.org/10.5194/angeo-36-1081-2018>.
- Borovsky, J.E., Valdivia, J.A., 2018. The Earth's magnetosphere: a systems science overview and assessment. *Surv. Geophys.* 39, 817–859. <https://doi.org/10.1007/s10712-018-9487-x>. <http://link.springer.com/10.1007/s10712-018-9487-x>.
- Brizard, A.J., Halm, T.S., 2007. Foundations of nonlinear gyrokinetic theory. *Rev. Mod. Phys.* 79, 421–468, 10.1103/RevModPhys.79.421. <https://link.aps.org/doi/10.1103/RevModPhys.79.421>.
- Burgess, D., Lucek, E.A., Scholer, M., Bale, S.D., Balikhin, M.A., Balogh, A., Horbury, T.S., Krasnoselskikh, V.V., Kucharek, H., Lembège, B., Möbius, E., Schwartz, S.J., Thomsen, M.F., Walker, S.N., 2005. Quasi-parallel shock structure and processes. *Space Sci. Rev.* 118, 205–222, 10.1007/s11214-005-3832-3. <http://link.springer.com/10.1007/s11214-005-3832-3>.
- 318–10 Chen, Y., Tóth, G., Cassak, P., Xia, X., Gombosi, T.I., Slavin, J.A., Markidis, S., Peng, I.B., Jordanova, V.K., Henderson, M.G., 2017. Global three-dimensional simulation of Earth's dayside reconnection using a two-way coupled magnetohydrodynamics with embedded particle-in-cell model: initial results. *J. Geophys. Res.: Space Physics* 122 (10), 335, 10.1002/2017JA024186. <https://agupubs.onlinelibrary.wiley.com/doi/abs/10.1002/2017JA024186>.
- Daldrorf, L.K.S., Tóth, G., Gombosi, T.I., Lapenta, G., Amaya, J., Markidis, S., Brackbill, J. U., 2014. Two-way coupling of a global Hall magnetohydrodynamics model with a local implicit particle-in-cell model. *J. Comput. Phys.* 268, 236–254.
- Fatemi, S., Poppe, A.R., Delory, G.T., Farrell, W.M., 2017. AMITIS: a 3D GPU-based hybrid-PIC model for space and plasma physics. *J. Phys. Conf. Ser.* 837, 012017, 10.1088/1742-6596/837/1/012017. <https://iopscience.iop.org/article/10.1088/1742-6596/837/1/012017>.
- Halekas, J., Delory, G., Brain, D., Lin, R., Mitchell, D., 2008. Density cavity observed over a strong lunar crustal magnetic anomaly in the solar wind: a mini-magnetosphere? *Planet. Space Sci.* 56, 941–946.
- Harned, D., 1982. Quasineutral hybrid simulation of macroscopic plasma phenomena. *J. Comp. Phys.* 47, 452–462.
- Hewett, D., 1980. A global method of solving the electron-field equations in a zero-inertia-electron-hybrid plasma simulation code. *J. Comp. Phys.* 38, 378–395.
- Ho, A., Datta, I.A.M., Shumlak, U., 2018. Physics-based-adaptive plasma model for high-fidelity numerical simulations. *Front. Phys.* 6, 105. <https://doi.org/10.3389/fphy.2018.00105>.
- Holmström, M., Fatemi, S., Futaana, Y., Nilsson, H., 2012. The interaction between the Moon and the solar wind. *Earth Planets Space* 64, 237–245.
- Kajdić, P., Blanco-Cano, X., Omid, N., Meziane, K., Russell, C.T., Sauvaud, J.-A., Dandouras, I., Lavraud, B., 2013. Statistical study of foreshock cavitons. *Ann. Geophys.* 31, 2163–2178, 10.5194/angeo-31-2163-2013. <https://www.ann-geophys.net/31/2163/2013/>.
- Kallio, E., 2005. Formation of the lunar wake in quasi-neutral hybrid model. *Geophys. Res. Lett.* 32, L06107. <https://doi.org/10.1029/2004GL021989>.
- Kallio, E., Dyadechkin, S., Wurz, P., Khodachenko, M., 2019. Space weathering on the Moon: farside-nearside solar wind precipitation asymmetry. *Planet. Space Sci.* 160, 9–22.
- Karimabadi, H., Vu, H., Krauss-Varban, D., Omelchenko, Y., 2006. Global hybrid simulations of the Earth's magnetosphere. In: Zank, G., Pogorelov, N. (Eds.), *Numerical Modeling of Space Plasma Flows*, Volume 359 of *Astronomical Society of the Pacific Conference Series*, p. 257.
- Karimabadi, H., Loring, B., Vu, H., Omelchenko, Y., Tatineni, M., Majumdar, A., Ayachit, U., Geveci, B., 2011. Petascale global kinetic simulations of the magnetosphere and visualization strategies for analysis of very large multi-variate data sets. In: Pogorelov, N., Audit, E., Zank, G. (Eds.), *5th International Conference of Numerical Modeling of Space Plasma Flows (ASTRONUM 2010)*, Volume 444 of *Astronomical Society of the Pacific Conference Series*, p. 281.
- Karimabadi, H., Roytershteyn, V., Vu, H.X., Omelchenko, Y.A., Scudder, J., Daughton, W., Dimmock, A., Nykyri, K., Wan, M., Sibeck, D., Tatineni, M., Majumdar, A., Loring, B., Geveci, B., 2014. The link between shocks, turbulence, and magnetic reconnection in collisionless plasmas. *Phys. Plasmas* 21. <https://doi.org/10.1063/1.4882875>. <http://scitation.aip.org/content/aip/journal/pop/21/6/10.1063/1.4882875>.
- Lin, Y., 2003. Global-scale simulation of foreshock structures at the quasi-parallel bow shock. *J. Geophys. Res.* 108, 1390. <http://doi.wiley.com/10.1029/2003JA009991>. <https://doi.org/10.1029/2003JA009991>.
- Lin, Y., Wang, X.Y., 2005. Three-dimensional global hybrid simulation of dayside dynamics associated with the quasi-parallel bow shock. *J. Geophys. Res.: Space Physics* 110, 1–13. <https://doi.org/10.1029/2005JA011243>.
- Lu, Q., Wang, H., Wang, X., Lu, S., Wang, R., Gao, X., Wang, S., 2020. Turbulence-driven magnetic reconnection in the magnetosheath downstream of a quasi-parallel shock: a three-dimensional global hybrid simulation. *Geophys. Res. Lett.* 47, 1–6. <https://doi.org/10.1029/2019GL085661>.
- Omelchenko, Y.A., Karimabadi, H., 2012a. HYPERS: a unidimensional asynchronous framework for multiscale hybrid simulations. *J. Comput. Phys.* 231, 1766–1780, 10.1016/j.jcp.2011.11.004. <https://linkinghub.elsevier.com/retrieve/pii/S0021999111006462>.
- Omelchenko, Y.A., Karimabadi, H., 2012b. Spontaneous generation of a sheared plasma rotation in a field-reversed  $\theta$ -pinch discharge. *Phys. Rev. Lett.* 109, 065004. <https://doi.org/10.1103/PhysRevLett.109.065004>.
- Omid, N., 2007. Formation of cavitons in the foreshock. In: *AIP Conference Proceedings*, vol. 932, pp. 181–190. <https://doi.org/10.1063/1.2778962>.
- Omid, N., Blanco-Cano, X., Russell, C.T., 2005. Macrostructure of collisionless bow shocks: 1. Scale lengths. *J. Geophys. Res.: Space Physics* 110. <https://doi.org/10.1029/2005JA011169>.
- Omid, N., Zhang, H., Sibeck, D., Turner, D., 2013. Spontaneous hot flow anomalies at quasi-parallel shocks: 2. Hybrid simulations. *J. Geophys. Res.: Space Physics* 118, 173–180. <http://doi.wiley.com/10.1029/2012JA018099>. <https://doi.org/10.1029/2012JA018099>.
- Omid, N., Zhou, X.Y., Russell, C.T., Angelopoulos, V., 2019a. The dominant role of energetic ions in solar wind interaction with the moon. *J. Geophys. Res.: Space Physics* 124, 3176–3192, 10.1029/2018JA026243. <https://onlinelibrary.wiley.com/doi/abs/10.1029/2018JA026243>.
- Omid, N., Zhou, X., Russell, C.T., Angelopoulos, V., 2019b. Reply to: comment on the dominant role of energetic ions in solar wind interaction with the moon by Poppe. *J. Geophys. Res.: Space Physics* 124, 6933–6937, 10.1029/2019JA026939. <https://onlinelibrary.wiley.com/doi/abs/10.1029/2019JA026939>.
- Plaschke, F., Hietala, H., Archer, M., Blanco-Cano, X., Kajdić, P., Karlsson, T., Lee, S., Omid, N., Palmroth, M., Roytershteyn, V., Schmid, D., Sergeev, V., Sibeck, D., 2018. Jets downstream of collisionless shocks. *Space Sci. Rev.* 214. <https://doi.org/10.1007/s11214-018-0516-3>.
- Poppe, A.R., 2019. Comment on “the dominant role of energetic ions in solar wind interaction with the moon” by omid et al. *J. Geophys. Res.: Space Physics* 124, 6927–6932. <https://doi.org/10.1029/2019JA026692>.
- Poppe, A.R., Fatemi, S., Halekas, J.S., Holmström, M., Delory, G.T., 2014. ARTEMIS observations of extreme diamagnetic fields in the lunar wake. *Geophys. Res. Lett.* 41, 3766–3773. <https://doi.org/10.1002/2014GL060280>.
- Raeder, J., 2003. Global magnetohydrodynamics, A tutorial. In: Büchner, J., Scholer, M., Dum, C.T. (Eds.), *Space Plasma Simulation*. Springer Berlin Heidelberg, Berlin, Heidelberg, pp. 212–246.
- Ridley, A.J., De Zeeuw, D.L., Rastätter, L., 2016. Rating global magnetosphere model simulations through statistical data-model comparisons. *Space Weather* 14, 819–834. <http://doi.wiley.com/10.1002/2016SW001465>. <https://doi.org/10.1002/2016SW001465>.
- Schwartz, S.J., Sibeck, D., Wilber, M., Meziane, K., Horbury, T.S., 2006. Kinetic aspects of foreshock cavitons. *Geophys. Res. Lett.* 33, L12103. <http://doi.wiley.com/10.1029/2005GL025612>. <https://doi.org/10.1029/2005GL025612>.
- Strumik, M., Roytershteyn, V., Karimabadi, H., Stasiwicz, K., Grzesiak, M., Przepiórka, D., 2015. Identification of the dominant ULF wave mode and generation mechanism for obliquely propagating waves in the Earth's foreshock. *Geophys. Res. Lett.* 42. <https://doi.org/10.1002/2015GL064915>.
- Sugiyama, T., Kusano, K., 2007. Multi-scale plasma simulation by the interlocking of magnetohydrodynamic model and particle-in-cell kinetic model. *J. Comput. Phys.*



- 227, 1340–1352. <https://doi.org/10.1016/j.jcp.2007.09.011>. <http://www.sciencedirect.com/science/article/pii/S0021999107003968>.
- Swift, D.W., 1996. Use of a hybrid code for global-scale plasma simulation. *J. Comput. Phys.* 126, 109–121, 10.1006/jcph.1996.0124. <http://www.sciencedirect.com/science/article/pii/S0021999196901242>.
- Tóth, G., Jia, X., Markidis, S., Peng, I.B., Chen, Y., Daldorff, L.K.S., Tenishev, V.M., Borovikov, D., Haiducek, J.D., Gombosi, T.I., Gloer, A., Dorelli, J.C., 2016. Extended magnetohydrodynamics with embedded particle-in-cell simulation of Ganymede's magnetosphere. *J. Geophys. Res.: Space Physics* 121, 1273–1293. <https://agupubs.onlinelibrary.wiley.com/doi/pdf/10.1002/2015JA021997>. arXiv: doi:10.1002/2015JA021997. <https://agupubs.onlinelibrary.wiley.com/doi/abs/10.1002/2015JA021997>.
- Turc, L., Ganse, U., Pfau-Kempf, Y., Hoilijoki, S., Battarbee, M., Juusola, L., Jarvinen, R., Brito, T., Grandin, M., Palmroth, M., 2018. Foreshock properties at typical and enhanced interplanetary magnetic field strengths: results from hybrid-vlasov simulations. *J. Geophys. Res.: Space Physics* 123, 5476–5493. <http://doi.wiley.com/10.1029/2018JA025466>. doi:10.1029/2018JA025466.
- von Alfthan, S., Pokhotelov, D., Kempf, Y., Hoilijoki, S., Honkonen, I., Sandroos, A., Palmroth, M., 2014. Vlasior: first global hybrid-Vlasov simulations of Earth's foreshock and magnetosheath. *J. Atmospheric and Solar-Terrest. Phys* 120, 24–35.
- Wang, L., Hakim, A.H., Bhattacharjee, A., Germaschewski, K., 2015. Comparison of multi-fluid moment models with particle-in-cell simulations of collisionless magnetic reconnection. *Phys. Plasmas* 22. <https://doi.org/10.1063/1.4906063>. <http://scitation.aip.org/content/aip/journal/pop/22/1/10.1063/1.4906063>.
- Wang, L., Germaschewski, K., Hakim, A., Dong, C., Raeder, J., Bhattacharjee, A., 2018. Electron physics in 3-D two-fluid 10-moment modeling of Ganymede's magnetosphere. *J. Geophys. Res.: Space Physics* 123, 2815–2830. <https://doi.org/10.1002/2017JA024761>.
- Winske, D., Yin, L., Omid, N., Karimabadi, H., Quest, K., 2003. Hybrid simulation codes: past, present and future - a tutorial. In: Büchner, J., Scholer, M., Dum, C.T. (Eds.), *Space Plasma Simulation, Volume 615 of Lecture Notes in Physics*. Springer Berlin Heidelberg, Berlin, Heidelberg, pp. 136–165. [https://doi.org/10.1007/3-540-36530-3\\_8](https://doi.org/10.1007/3-540-36530-3_8).
- Zhang, H., Khurana, K., Kivelson, M., Fatemi, S., Holmström, M., Angelopoulos, V., Jia, Y., Wan, W., Liu, L., Chen, Y., Le, H., Shi, Q., Liu, W., 2016. Alfvén wings in the lunar wake: the role of pressure gradients. *J. Geophys. Res.* 121, 10698–10711. <https://doi.org/10.1002/2016JA022360>.